Predissociation dynamics of the O_2 $B\ ^3\Sigma_u^-$ state: Vibrational state dependence of the product fine-structure distribution

David J. Leahy,[a] David L. Osborn,[b] Douglas R. Cyr,[c] and Daniel M. Neumark[d]
Department of Chemistry, University of California, Berkeley, California 94720,
and Chemical Sciences Division, Lawrence Berkeley Laboratory, Berkeley, California 94720

(Received 14 April 1995; accepted 9 May 1995)

The predissociation of the $O_2B\ ^3\Sigma_u^-$ state (v=0–11) is investigated using fast beam photofragment translational spectroscopy. The energy resolution of the experiment, 7–10 meV, is sufficient to yield the *correlated* fine structure distribution $P(j_1,j_2)$ for the two $O(^3P_j)$ fragments. These spin–orbit branching ratios depend markedly on the vibrational quantum number, providing detailed insight into a relatively unexplored facet of molecular dissociation dynamics. No less than four repulsive states are expected to mediate the predissociation of the $B\ ^3\Sigma_u^-$ state, primarily via spin–orbit coupling, and the couplings among these states at long range ($R\sim$5–7 Å) determine the final spin–orbit distributions $P(j_1,j_2)$. We have attempted to model these distributions in both the adiabatic and diabatic limits, with neither limit proving very successful. A more phenomenological approach to fitting our data suggests that products with $j_1=j_2=2$ result from single transitions between adiabatic potentials at long range, whereas the populations in the other product states are determined by multiple transitions among the repulsive states. © *1995 American Institute of Physics.*

I. INTRODUCTION

Since the origins of molecular spectroscopy, the Schumann–Runge $B\ ^3\Sigma_u^-(v')\leftarrow X\ ^3\Sigma_g^-(v'')$ bands of molecular oxygen have received a great deal of well-deserved attention.[1–20] The long progression of rotationally resolved vibrational bands provides a textbook example of the electronic excitation of a homonuclear diatomic molecule. Moreover, the photochemistry and photophysics of the $B\ ^3\Sigma_u^-$ state of oxygen have important practical ramifications for the chemistry of the earth's atmosphere. The Schumann–Runge bands are the dominant absorbers of solar ultraviolet light in the wavelength range from 180 to 205 nm. The penetration depth of this photochemically important radiation into the earth's atmosphere depends sensitively on the details of the $B\ ^3\Sigma_u^-(v')\leftarrow X\ ^3\Sigma_g^-(v'')$ spectrum, particularly on the natural linewidths.

In 1936, Flory reported that the irradiation of O_2 with a mercury lamp at 184.5 nm led to the photochemical production of ozone, and was the first to suggest that the $B\ ^3\Sigma_u^-$ state was predissociated by the repulsive $^3\Pi_u$ state to form a pair of $O(^3P_j)$ atoms.[21] Some controversy ensued over this issue for decades. However, since the work of Wilkinson and Mulliken,[5] it has been known that the $B\ ^3\Sigma_u^-$ state predissociates with near unity quantum efficiency. The resulting oxygen atoms are responsible for the formation of ozone in the upper atmosphere via three-body collisions. The reverse process, $O(^3P_j)$ atom recombination, forms highly excited O_2 molecules,[22–25] which may radiate (this process is presumed to make up much of the terrestrial atmosphere nightglow), electronically activate other species in collisions, or possibly even react with O_2 to form ozone.[26,27] Oxygen atom recombination is a formidably complicated process because it involves the collision of two open shell atoms. While some progress has been made, definitive experimental information is sparse, and it remains to be proven which molecular potential states are the most important.[28]

In this paper, we investigate the predissociation of the 12 lowest vibrational levels of the O_2 $B\ ^3\Sigma_u^-$ state by measuring the photofragment energy distribution resulting from the photodissociation of a fast (5 keV) beam of O_2. Vibrationally excited O_2 in its ground $X\ ^3\Sigma_g^-$ state is generated by photodetachment of a fast beam of O_2^- anions. The O_2 is excited to various predissociating levels of the $B\ ^3\Sigma_u^-$ state, and the resulting O atoms are detected using a coincidence detection scheme which yields high kinetic energy resolution for the photofragments (7–10 meV). Our experiment shares some features in common with previous studies of O_2 photodissociation by van der Zande[29] and Cosby,[30] in which excited O_2 was generated by charge transfer neutralization of O_2^+.

The resolution of our instrument is sufficiently high to reveal the *correlated* spin–orbit distributions $P(j_1,j_2)$ of the pair of product $O(^3P_j)$ atoms. This sort of measurement is largely unprecedented and provides a new perspective into diatomic photodissociation dynamics, as well as the reverse process, collisions of open shell atoms. Because the products are a pair of atoms with only electronic degrees of freedom, the process of diatomic molecule dissociation appears so basic that one might expect an uncomplicated model to provide predictive power of the product state distributions. However, the results presented in this paper show that this is not the case, and that the simple molecular dissociation system $O_2B\ ^3\Sigma_u^-(v')\rightarrow O(^3P_{j_1}), O(^3P_{j_2})$ is sufficiently complex to defy any straightforward explanation.

Figure 1 shows the potential energy curves for the O_2

[a]Current address: Worlds, 510 Third St., Suite 530, San Francisco, CA 94107.
[b]NDSEG Predoctoral Fellow.
[c]Current address: Combustion Research Facility, Sandia National Laboratories, Livermore, CA 94550.
[d]Camille and Henry Dreyfus Teacher–Scholar.

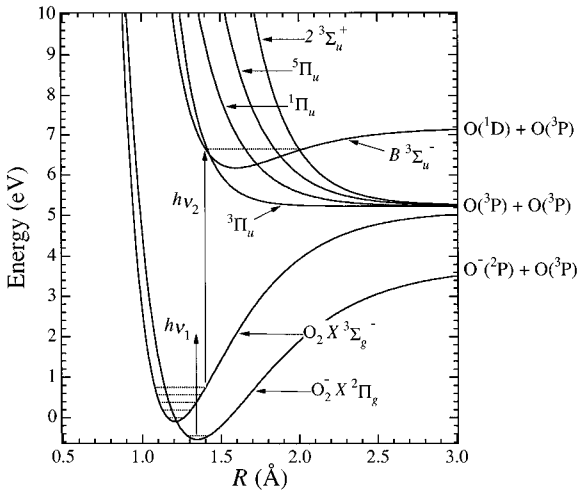

FIG. 1. Diagram of relevant potentials surfaces of O_2 and O_2^-.

states most relevant to our experiment. The open shell $(1\pi_g)^2$ structure of ground state O_2, together with the relatively high multiplicity of the ground state photodissociation products [i.e., a pair of $O(^3P_j)$ atoms], results in a great richness of low-lying O_2 electronic states. With this in mind, it comes as no surprise that the $B\ ^3\Sigma_u^-$ state, which correlates asymptotically to the $O(^1D)$,$O(^3P_j)$ limit, is crossed by a large number of repulsive states that correlate to the ground state products. In Fig. 1, only the four dissociative states believed to contribute significantly to predissociation of the $B\ ^3\Sigma_u^-$ state are shown; in fact, there are no less than *ten* repulsive curves that cross this state on the way to the $O(^3P_{j_1})$,$O(^3P_{j_2})$ limit. In addition, several bound states correlate to this atomic limit.

The product state distributions $P_v(j_1,j_2)$ obtained from our experiment are complementary to the extensive and continuing body of research into the predissociation-induced broadening of the $B\ ^3\Sigma_u^-(v')\leftarrow X\ ^3\Sigma_g^-(v'')$ absorption spectrum. Following Wilkinson and Mulliken's original observation, it has long been observed that the natural linewidths of the Schumann–Runge bands have a strong v' dependence.[5,6,8] The lines are especially sharp for $v'=0$, reach a maximum in width for $v'=4$, and show some oscillations in width to higher v'. Murrell and Taylor[31] showed that the application of the Franck–Condon principle leads to the idea that a single curve crossing between the repulsive $^3\Pi_u$ state and the outer limb of the B state can account for the v' dependence of the predissociation rate. Schaefer and Miller[32] later proposed that three repulsive states, namely, the $^1\Pi_u$, $^3\Pi_u$, and $^5\Pi_u$ states, all play important roles in the predissociation of the $B\ ^3\Sigma_u^-$ state. They deduced that the primary predissociation mechanism is spin–orbit coupling between the B state and those repulsive states which are connected by the first-order spin–orbit selection rules $\Delta\Omega=0$, $\Delta\Lambda=-\Delta\Sigma=0$, ±1 (also, $g\leftarrow/\rightarrow u$ and $\Sigma^+\leftrightarrow\Sigma^-$).[33] Their electronic structure calculations showed that the $^3\Pi_u$ crossed the *inner* limb of the B state, while the $^1\Pi_u$ state and $^5\Pi_u$ state were predicted to cross the outer limb. Julienne and Krauss[34] supported these conclusions at a higher level of theory; Julienne[35] went on to point out that there is also a strong spin-orbit interaction with the $2\ ^3\Sigma_u^+$ state, which crosses the $B\ ^3\Sigma_u^-$ state at a somewhat larger internuclear distance R.

The calculations in Refs. 34 and 35 were of sufficient accuracy to provide qualitative numbers for the crossing points R_x and slopes M_x of the repulsive curves, as well as values for A_x, the strengths of the spin–orbit couplings. However, their Franck–Condon calculation of the predissociation widths based on their curve-crossing parameters agreed only qualitatively with the best spectroscopic linewidths available at the time.[6,8] The agreement did not improve under the scrutiny of higher resolution spectra,[12,13,16] and two separate research groups have taken semiempirical approaches to adjust the characteristics of the curve crossings to improve the agreement between experiment and theory.[11,15,19,20] These efforts have culminated in refined values for the R_x, M_x, and A_x parameters that are consistent with experiment. These new curve-crossing parameters are in close enough agreement with the purely *ab initio* values that it is safe to conclude that the theoretical framework for the mechanism proposed by Schaefer and Miller and expanded by Julienne and Krauss is essentially correct. The results of the semiempirical models thus provide relatively reliable partial cross sections for dissociation onto the $^5\Pi_u$, $^3\Pi_u$, $^1\Pi_u$, and $2\ ^3\Sigma_u^+$ states as a function of v'.

While these earlier studies have focused on the mechanism of the initial curve crossings, our experiment sheds light on a second, equally fundamental problem, namely, how these repulsive states project onto the atomic oxygen spin–orbit states (j_1,j_2). The uncorrelated fine structure branching ratios have been measured for predissociation of the $B\ ^3\Sigma_u^-$ state to $O(^3P)+O(^3P)$ and, at higher energy, direct dissociation to $O(^1D)+O(^3P)$.[36–38] In a recent publication,[39] we reported the first measurements of correlated spin–orbit populations $P(j_1,j_2)$ arising from the predissociation of a selected vibration–rotation level of the O_2 $B\ ^3\Sigma_u^-$ state, the $(v=7, N=4)$ level. In this paper, we extend our earlier work to the $(v=0$–$11, N=4)$ levels of the O_2 $B\ ^3\Sigma_u^-$ state. The correlated fine structure distributions show a marked dependence on the vibrational quantum number in the $B\ ^3\Sigma_u^-$ state, showing that the detailed predissociation mechanism depends strongly on v.

Our results will be presented in terms of two simple limiting cases for evolution of the molecule to the atomic asymptotes. One limit, the "relativistic adiabatic" model, predicts the product states on the assumption the atoms recoil infinitely slowly with respect to the electronic motion. The second model approaches the problem from the opposite direction: It predicts atomic state distributions in the "sudden limit," where the molecular states are projected onto the atomic states without account for the evolution of the electronic wave function during the dissociation. The validity of these two limits will be discussed in the context of O_2 dissociation. We also present a more phenomenological analysis that provides further insights into how the repulsive states $^1\Pi_u$, $^3\Pi_u$, $^5\Pi_u$, and $2\ ^3\Sigma_u^+$ project onto the asymptotic limits (j_1,j_2). The varying degrees of success of these simple models show that the observed branching ratios $P(j_1,j_2)$ are the end result of a richly dynamical process.

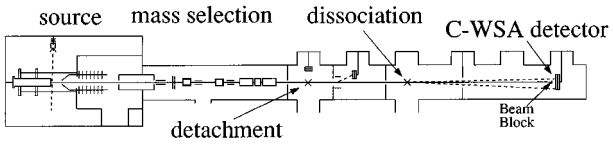

FIG. 2. Schematic of the experimental apparatus. The C-WSA (coincidence wedge-and-strip anode) detector is discussed in the text.

II. EXPERIMENT

A. Experimental method

The principle of the experiment is as follows. We form a fast, mass-selected beam of O_2^-, photodetach the ions to form fast neutral O_2, excite a predissociative transition in O_2 with a second laser pulse, and measure the recoil of the resulting pair of O atoms. The experimental method was presented in some depth in Ref. 40, and a relatively brief description will be presented here. A schematic of the experimental apparatus is shown in Fig. 2.

The experiment utilizes a pulsed ion source together with two pulsed laser systems, operating at a repetition rate of 60 Hz. In the source region, a beam of internally cold O_2^- anions is formed by crossing a pulsed supersonic expansion of neat O_2 with a continuous 1 keV electron beam. The relatively slow secondary electrons from electron impact ionization form negative ions via dissociative attachment; dissociation of van der Waals dimers or larger clusters is presumably the mechanism for O_2^- formation. These ions are skimmed, collinearly accelerated to 5 keV, and collimated with an einzel lens. The resulting fast beam of ions is re-referenced to ground potential by means of an "ion elevator;"[41,42] this feature enables the pulsed valve source and the detector to be simultaneously referenced to ground. Just after exiting the ion elevator, the beam is chopped by a transverse beam modulator,[43] forming a packet of ions which separate in a time-of-flight region according to mass. The O_2^- anions are photodetached by a loosely focused pulsed laser beam (1 mm diameter spot size) at 480 nm from an excimer-pumped dye laser. Figure 1 shows there is a significant decrease in equilibrium bond length on the transition from anion to neutral. As a result, the O_2 neutrals are formed in a strongly inverted vibrational state distribution[44,45] while remaining rotationally cold. In addition, some $a\ ^1\Delta_g$ oxygen is formed by photodetachment, but our experiment is insensitive to these molecules.

The resulting 5 keV beam of vibrationally excited O_2 neutrals is intercepted by a second pulsed laser beam, which excites specific O_2 $B\ ^3\Sigma_u^-(v',N') \leftarrow X\ ^3\Sigma_g^-(v'',N'')$ transitions. This laser pulse is formed by frequency doubling the output of a second excimer-pumped dye laser system in a BBO crystal. The wavelengths used in this work range from 206.04 nm for the $B\ ^3\Sigma_u^-(v'=9) \leftarrow X\ ^3\Sigma_g^-(v''=4)$ transition up to 239.17 nm for the $v'=0 \leftarrow v''=5$ transition. The transitions were chosen according to the Franck–Condon factors tabulated in Ref. 8. The linewidth of the frequency doubled light is typically 0.4 cm^{-1}. The electronically excited molecules go on to predissociate into a pair of photofragments. The lifetimes of the excited molecules depend strongly on v', but they all fall in the range from 1.2 to 50 ps (the natural linewidths range from 0.1 to 4 cm^{-1}).[16,18,20] These lifetimes are sufficiently short that the predissociation is essentially instantaneous when compared to the 5.8 μs flight time of the fragments through the 1 m drift region. (This was extended to 2 m for the $v'=2$ data set; see below.)

The photofragment detection scheme is based on the method developed by DeBruijn and Los[46] and involves the observation of both fragments in coincidence. While the vast majority of the neutrals are not dissociated and impinge on a beam block, each pair of photofragments recoils out of the beam onto the active area of a time- and position-sensitive detector located 1 m downstream from the dissociation laser (as depicted by the dotted lines in Fig. 2). By scanning the wavelength of the photodissociation laser, we can record the dissociative spectroscopy of the neutrals. The primary mode of operation of the machine, however, is to study the translational energy release following the photodissociation of free radicals. Our detector can record in coincidence the time and position of the arrival of each of the two photofragments belonging to a single parent radical.[40] By collecting several thousand coincident events, we can accumulate the energy- and angle-resolved spectrum of the photofragments for any given photodissociation wavelength.

For each observed coincidence event, the photofragment detector records the impact positions of both fragments with an accuracy of about 100 μm (see the following subsection for a description of the position-sensitive data analysis). Simultaneously, we use a time-to-amplitude converter to record the time interval between the arrival of the two fragments to an accuracy of 500 ps. Together, these measurements yield the center-of-mass translational energy release and the recoil angle of each photodissociation event. For fragments of equal mass (as in the case of O_2), these relationships are given by

$$E_{\text{c.m.}} = \frac{1}{2} E_{\text{beam}} \frac{R_{xy}^2 + (v_{\text{beam}} \Delta t)^2}{L^2} \tag{1}$$

and

$$\theta = \arctan\left(\frac{R_{xy}}{v_{\text{beam}} \Delta t} \right), \tag{2}$$

where E_{beam} and v_{beam} are the laboratory energy and velocity of the O_2 beam, respectively; R_{xy} is the observed recoil distance perpendicular to the beam axis (as measured by the position-sensitive detector); Δt is the time interval between the arrivals of the two photofragments at the detector; and L is length of the drift region.

The kinetic energy resolution for data collected with a 1 m photofragment flight length was 9–12 meV for recoil energies ranging from 1.0 to 1.75 eV. Photodissociation of one level ($v'=2$) was reinvestigated with a 2 m drift region; this experiment produced our best resolution to date, with peaks of 6.8 meV FWHM at a recoil energy of 1.15 eV ($\Delta E_{\text{c.m.}}/E_{\text{c.m.}}=0.6\%$). The resolution is determined by the precision to which R_{xy} and Δt are determined; the contribution from the kinetic energy spread in the radical beam is negligible, as $\Delta E_{\text{beam}}/E_{\text{beam}} < 0.1\%$. As pointed out previously,[39,46] the high resolution of this experiment results

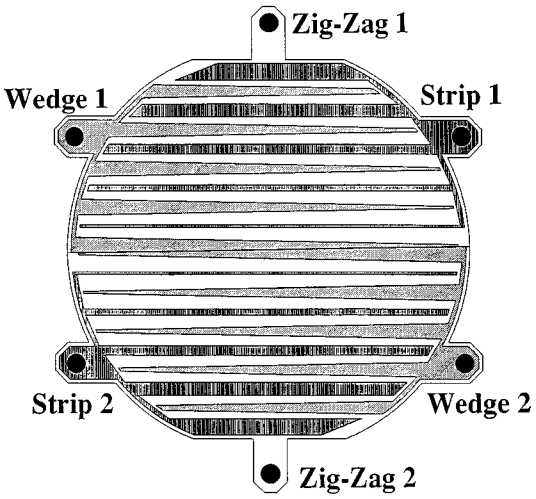

FIG. 3. Schematic of the wedge-and-strip anode. The five-period pattern shown is to illustrate the structure of the anodes; the actual anode has 32 periods per half. The terminal for the wedge, strip, and zig–zag conductors on both halves of the anode are indicated in the figure. The solid lines between the conductors represents the insulating gaps.

from the detection of the photofragments in coincidence, so that broadening effects due to the spatial and temporal spread of the radical beam largely cancel out.

While the fast-beam coincidence detection scheme has its advantages, it also gives rise to the serious constraint that we may record only one coincidence event per laser shot. Together with our 25% coincidence detection efficiency (i.e., ~50% for each fragment), our maximum coincidence detection rate is around 10% of the experimental repetition rate of 60 Hz. In the oxygen experiments presented in this paper, we typically recorded 2–4 coincident events per second, allowing the collection of a typical 50 000 event data set in a few hours' time.

B. Position-sensitive data analysis

We have recently devoted considerable effort towards optimizing the accuracy of the time- and position-sensitive detector. For this reason, our data analysis scheme will be described in some detail. The fragment impact positions are observed by using of a pair of wedge-and-strip anodes that collect the charge from the detector's microchannel plates.[40,47] A schematic of the wedge-and-strip anode pattern is shown in Fig. 3; the actual pattern is considerably denser. This pattern consists of two separate wedge-and-strip anodes (one upper and one lower, which we will label 1 and 2, respectively), comprised of three conductors each (''wedge,'' ''strip,'' and ''zigzag''). These anodes divide the $\sim 10^7$ electrons from the microchannel plates between the three conductors in a spatially specific manner. The wedge conductor tapers in the horizontal direction while the strip conductor changes in width along the vertical direction, so the two electrodes determine the horizontal and vertical position, respectively, of the centroid of the electron cloud. The following equations relate these charge fractions to the impact positions:

$$x_1 = a_{1x} F_{\text{wedge}} + b_{1x}, \tag{3a}$$

$$y_1 = a_{1y} F_{\text{strip}} + b_{1y} + c_{1y} F_{\text{strip}}^2, \tag{3b}$$

$$x_2 = a_{2x} F_{\text{wedge}} + b_{2x}, \tag{3c}$$

$$y_2 = a_{2y} F_{\text{strip}} + b_{2y} + c_{2y} F_{\text{strip}}^2. \tag{3d}$$

The Cartesian coordinates x and y are the horizontal and vertical positions, respectively, of the fragment impacts relative to the origin, which we define to lie at the center of the radical beam. The multiplicative constants a_k and additive constants b_k define the nearly linear relationship between the anode charge fractions F and the Cartesian coordinates. In addition, we have included a small quadratic term in the y coordinate equations to model an inherent nonlinearity in the detector's charge division. Equations (3a)–(3d) are different and somewhat simpler than those that appear in Ref. 40; for our charge amplification scheme, the cross-talk corrections have proven to be of negligible importance. The crux of the data analysis is the determination of the values of the parameters a_k, b_k, and c_k. While rough guesses for a_k and b_k can be made based on the anode geometry, in a quantitative analysis the ten constants appearing in Eqs. (3a)–(3d) must be determined from experimental data directly. We accomplish this by treating the constants as parameters in a nonlinear least squares fit to the oxygen data, with the merit function

$$\chi^2 = \sum_i \frac{(R_{\text{calc}} - R_{\text{obs},i})^2}{\sigma_{\text{recoil}}^2} + \frac{R_{\text{centroid},i}^2}{\sigma_{\text{centroid}}^2}, \tag{4}$$

where

$$R_{\text{obs},i} = [(x_1^i - x_2^i)^2 + (y_1^i - y_2^i)^2 + (v_{\text{beam}} \Delta t_i)^2]^{1/2} \tag{5}$$

and

$$R_{\text{centroid},i} = \{[(x_1^i + x_2^i)/2]^2 + [(y_1^i + y_2^i)/2]^2\}^{1/2}. \tag{6}$$

The index i stands for the independent coincident events. R_{calc} is the calculated recoil distance given by inverting Eq. (1) and using the known oxygen bond strength (5.117 eV, Ref. 48), the photon energy, the parent oxygen beam velocity v_{beam}, and the length of the fragment drift region. R_{calc} is first determined using the kinetic energy release corresponding to the ($j_1=2$, $j_2=1$) final state; this was the most probable state from predissociation of the $v'=7$ level.[39] In subsequent iterations, the mean kinetic energy release for each data set is used. R_{obs} is the length of the observed three dimensional recoil vector between the two fragments, which depends on the adjustable parameters a_k, b_k, and c_k. Similarly, R_{centroid} is the parameter-dependent distance from the center of the radical beam to the parent radical impact (as inferred from the fragment impacts, using conservation of momentum). The constants σ_{recoil} and σ_{centroid} characterize the standard deviations in the recoil measurements (150 μm; the detector's effective diameter is 40 mm) and centroid positions (namely, the radical beam width, which is 1.6 mm).

The nonlinear least squares fit utilizes a Levenberg–Marquardt algorithm.[49] The fit is provided with data sets of a few tens of thousands coincident events in the form of the raw charge fractions of Eqs. (3a)–(3d). Following an initial estimate, the adjustable parameters a_k, b_k, and c_k are optimized by the algorithm to minimize χ^2. This results in a set

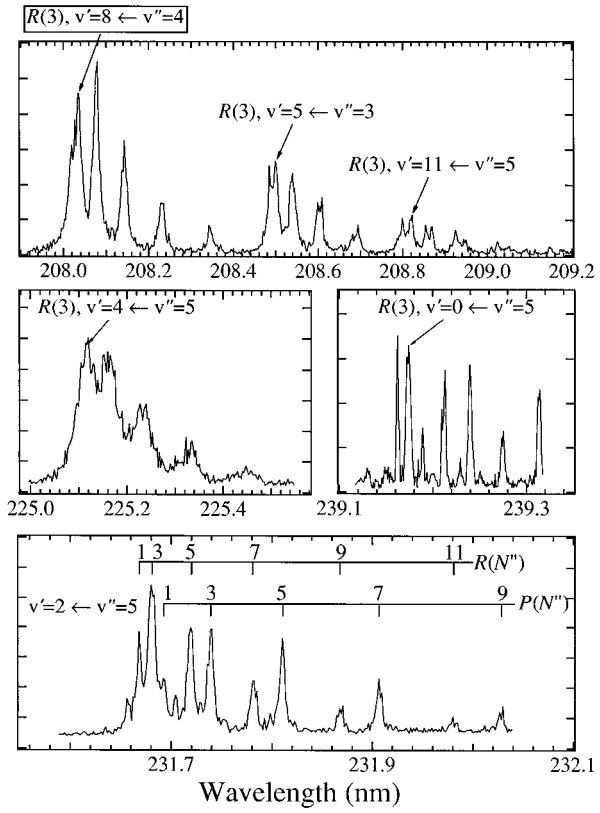

FIG. 4. Total photofragment yield wavelength scans for several bands of the Schumann–Runge $B\ ^3\Sigma_u^- \leftarrow X\ ^3\Sigma_g^-$ system.

of parameters that yield the high resolution kinetic energy release spectra presented in this work. In addition, the oxygen data fits provide an excellent absolute calibration for the position sensitive detector, which is an essential first step for our photodissociation studies of other polyatomic free radicals.[40,50,51]

III. RESULTS

Our experimental results can be grouped into three categories: wavelength scans, kinetic energy release (KER) spectra, and photofragment angular distributions. The wavelength scans allowed us to identify specific rovibrational transitions for subsequent dynamical study by our photofragment coincidence detection scheme. The KER spectra and the photofragment angular distributions are both derived from the coincidence data sets recorded at the selected excitation wavelengths. The angular distributions were found to exhibit saturation effects and will not be discussed here.

A sample of our scans of photofragment yield vs wavelength are shown in Fig. 4. The spectra are rotationally resolved and were easily assigned. It is clear from Fig. 4 that the natural linewidths depend strongly on v', with $v'=0$ and 4 representing the narrow and broad extremes, respectively, in agreement with earlier results.[5,6,8] An analysis of the intensity distributions yielded a rotational temperature of 55 K for the neutral O_2 molecules. Since neutrals produced by photodetachment will have a slightly broader rotational distribution than the parent anions, the anion rotational temperature should be somewhat colder than this.

These spectra show all of the essential features of the Schumann–Runge bands. These bands are very strongly degraded to the red by the large increase in R_e from 1.21 Å in the $X\ ^3\Sigma_g^-$ state to 1.60 Å in the $B\ ^3\Sigma_u^-$ state. As a result, the R branch runs directly to the red and is strongly overlapped with the P branch for many bands. The R and P branch transitions are nominally labeled as $R(N'')$ and $P(N'')$, as shown in Fig. 4 for the $v'=2 \leftarrow v''=5$ band. However, all lines for which N'' and $N' \geqslant 1$ consist of at least three overlapping transitions with $\Delta J=\Delta N$ originating from the F_1, F_2, and F_3 fine structure components of the N'' rotational level. A few weak "case (a)" transitions for which $\Delta J \neq \Delta N$ [such as the ${}^RQ_{32}(1)$ transition] may be seen near the origin of the well-resolved $v'=0$ and 2 spectra.

Photodissociation kinetic energy release spectra were obtained by tuning the dissociation laser to the $R(3)$ transitions for all v'. This transition was chosen since it was typically the most intense for a vibrational band. The results are shown in Fig. 5 for $v'=0$–11, with the results for $v'=2$ expanded in Fig. 6. A small number of kinetic energy release spectra were obtained for other rotational transitions but were found to be virtually identical to the results in Fig. 5 (for the same v'). At sufficiently high N', one expects effects due to rotation–electronic coupling to appear in the predissociation dynamics,[20] but the cold rotational temperature in our beam precludes us from examining these levels.

The photofragment kinetic energy $E_{\text{c.m.}}$ is related to the desired quantity, namely, the internal energy of the photoproducts E_{int}, by

$$E_{\text{c.m.}}=E_{\text{int},0}+h\nu-D_0-E_{\text{int}}. \tag{7}$$

$E_{\text{int},0}$ and D_0 (5.117 eV) are the initial internal energy and the bond dissociation energy of the parent, respectively. $E_{\text{int},0}$ is determined by our choice of predissociation resonance, which selects specific rovibrational levels from the distribution of $X\ ^3\Sigma_g^-$ molecules in the fast beam. The fact that we excite a few overlapping rotational levels (as discussed in Sec. IV) adds 2 meV of energy uncertainty to $E_{\text{int},0}$. Because $E_{\text{int},0}$, D_0, and the photon energy $h\nu$ are known quantities, the internal energy E_{int} is obtained directly from the observed kinetic energy release.

The internal energy of the products in this case is limited to the oxygen atom $O(^3P_j)$ spin orbit levels: $j=1$ and $j=0$ lie 20 and 28 meV above the ground state $j=2$, respectively.[52] Formation of a pair of $O(^3P_j)$ atoms results in six energetically distinct (j_1,j_2) channels, with the ground state products $(j_1=2,\ j_2=2)$ appearing at highest kinetic energy. The kinetic energy resolution of the spectra shown in Fig. 5 is high enough for the structure associated with the correlated spin–orbit states (j_1,j_2) to be manifest. These states are labeled in the spectrum in Fig. 6. It is immediately clear that the fine-structure branching ratios depend strongly on the vibrational level prepared in the $B\ ^3\Sigma_u^-$ state. The clearest example of this dependence appears in the ground state channel (2,2), which is relatively well resolved from its nearest neighbor (2,1) by a 20 meV energy gap. The (2,2) peak is intense in the $v'=0$ and 1 spectra, appears more weakly for intermediate v', and recurs strongly in the $v'=8$ and 9 spectra. For all of the spectra, the most intense feature appears in

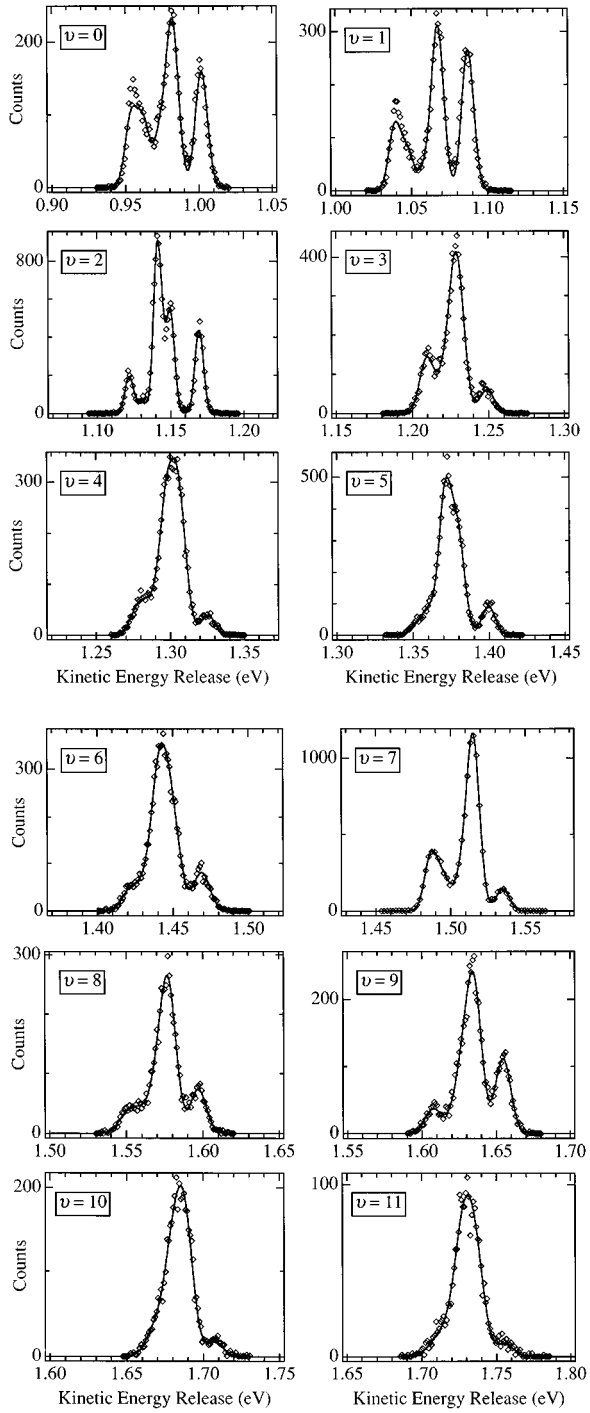

FIG. 5. Photofragment kinetic energy release for the predissociation of the $v'=0$ to 11 levels of the O_2 $B\ ^3\Sigma_u^-$ state. The circles represent the data, and the solid lines are the fits of the data to the correlated spin–orbit populations $P_v(j_1,j_2)$.

the middle of the spin–orbit distribution, corresponding to the partially overlapped (2,1) and (2,0) channels. A cursory analysis of the data also reveals that the most energetic of the open channels, the (0,0) channel, is completely absent in all of the observed kinetic energy releases.

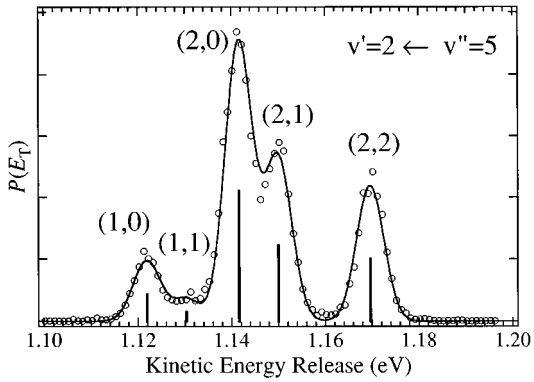

FIG. 6. Expanded view of photofragment kinetic energy release for the $v'=2$ level of the O_2 $B\ ^3\Sigma_u^-$ state.

IV. ANALYSIS

A. Correlated spin–orbit distributions

Following the method described in our recent communication,[39] we extracted quantitative branching ratios $P_v(j_1,j_2)$ from each of the spectra shown in Fig. 5 by fitting the data with Gaussian line shapes separated by $O(^3P_j)$ energies. In this fit, the intensity of each Gaussian was adjusted, as well as a common linewidth for all peaks. The absolute recoil energy scale was easily determined directly from the spectra, because the energy resolution of the data in Fig. 5 is sufficiently high that the pattern of energy spacings in the (j_1,j_2) products is evident; the (2,2) peaks are particularly prominent. The actual fitting procedure involved optimizing the nonlinear parameters (peakwidth and absolute energy) ''by hand,'' with a linear least-squares fit of the intensities of each peak being performed at each iteration. In all cases, the fits converged rapidly to give an unambiguous assignment of the spectral features to the correlated spin–orbit channels (j_1,j_2).

The results of the fits are given in Table I and are also shown in Fig. 5 as solid lines. The uncertainties in the branching ratios in the table are 1σ as derived from the least-squares fitting procedure. Because the features proved to be very well fit by the Gaussian line shapes, the branching ratios for even strongly overlapped product states such as (2,1) and (2,0) are fairly well determined. The data represented in Table I are the major result of this work, and the discussion in Sec. V is devoted to the information content in these vibrational state-dependent spin–orbit branching ratios.

B. Rotational level populations

In Sec. V, we will explore the relationship between the short-range predissociation mechanism and the observed spin–orbit distributions $P_v(j_1,j_2)$. To do so, it is important to characterize the levels of the $B\ ^3\Sigma_u^-$ state that we are accessing in our experiment. As discussed in Sec. III, the $R(3)$ transition that we are nominally exciting for each B state vibrational level v' actually consists of at least three overlapping transitions, namely, the $R_1(4)$, $R_2(3)$, and $R_3(2)$ transitions which originate from the three F_i fine-structure components of the $N''=3$ level with $J''=4$, 3, and 2, respectively. Moreover, for $v'\geqslant 4$, the individual linewidths are suf-

TABLE I. Correlated spin–orbit distributions $P_v(j_1,j_2)$ as a function of $B\ ^3\Sigma_u^-$ state vibrational level v'. No products were observed in the (0,0) state. Uncertainties are given inside parentheses.

v'	$P(2,2)$ (%)	$P(2,1)$ (%)	$P(2,0)$ (%)	$P(1,1)$ (%)	$P(1,0)$ (%)
0	25.2(1.2)	35.1(1.6)	11.0(1.3)	13.5(1.2)	15.2(1.1)
1	33.1(1.3)	38.3(1.5)	4.8(0.9)	8.7(0.9)	15.1(1.0)
2	20.4(0.7)	25.0(0.9)	42.1(1.1)	3.5(0.4)	8.9(0.5)
3	9.1(0.7)	58.3(2.0)	12.0(1.5)	20.3(1.2)	0.2(0.4)
4	5.9(0.6)	40.6(1.8)	37.8(2.0)	8.2(1.1)	7.6(0.8)
5	9.8(0.6)	32.6(1.4)	47.4(1.7)	8.1(0.8)	3.0(0.5)
6	13.0(0.8)	30.1(1.8)	44.8(2.2)	6.0(1.2)	6.0(0.8)
7	7.1(0.5)	55.8(1.6)	9.9(1.0)	9.6(0.9)	17.7(0.9)
8	16.6(1.1)	55.7(2.4)	14.5(2.0)	7.4(1.2)	5.8(0.9)
9	24.6(1.3)	48.1(2.3)	17.4(1.9)	2.7(1.0)	7.3(0.9)
10	5.4(0.8)	51.8(3.0)	33.3(3.0)	9.4(1.6)	0.2(0.6)
11	5.2(1.1)	39.4(4.1)	43.8(4.8)	8.0(2.7)	3.7(1.4)

ficiently broad so that the $P(1)$ and $^RQ_{32}(1)$ lines overlap the $R(3)$ transition. Finally, for the most diffuse bands such as $v'=4$, the $R(3)$ line overlaps additional transitions, especially the $R_1(3)$ and $R_2(2)$ transitions originating from the $N''=2$ rotational level.

These issues are important because the short range predissociation mechanism depends on the rotational fine structure through the Ω dependence of the coupling between the $B\ ^3\Sigma_u^-$ and the four repulsive states.[20,34,35] The F_2 levels consist purely of the $^3\Sigma_1(\Omega=1)$ component, while F_1 and F_3 are complementary mixes of the $\Omega=0$ and 1 components.[53] Only the $\Omega=1$ components of the $B\ ^3\Sigma_u^-$ state couple to the $^1\Pi_u$ and $2\ ^3\Sigma_u^+$ states. As a result, the F_2 fine-structure states have approximately twice the dissociation rate onto these two curves as do the F_1 and F_3 components belonging to the same v, N level. On the other hand, the $^5\Pi_u$ state couples to the three F_i components with almost equal strength, while, for low rotational levels, the $^3\Pi_u$ state couples somewhat more strongly to the $\Omega=0$ component of the $B\ ^3\Sigma_u^-$ state, thereby slightly disfavoring dissociation from the F_2 component. The overall effect is that the predissociation rates for the F_1, F_2, and F_3 fine structure components of a rotational level N' are all different. This is seen most dramatically in the experiments by Cosby *et al.*,[18] and is also evident in the work by Yang *et al.*[16] and Yoshino *et al.*[17] It is therefore very useful to know the fine-structure composition of each of the predissociating levels accessed in our experiment; this depends on which transitions are overlapped for each nominal $R(3)$ line.

We have simulated the excitation spectrum, taking into account the detailed spin–rotation structure and its effect on the rotational line strengths.[53] Using our spectrum simulation, we calculated the populations of overlapping spin–rotation levels $P_u(J,F_i)$ prepared in our experiment for each vibrational level. The simulation takes into account the exact linestrengths, line positions and linewidths of all possible transitions, in addition to the bandwidth of the excitation light. The result is a set of normalized fine-structure populations for each ensemble of transitions associated with the $B\ ^3\Sigma_u^-$ state vibrational level v

$$n_v(F_i)=\sum_J P_v(J,F_i) \Big/ \sum_{J,i} P_v(J,F_i). \tag{8}$$

The results may be summarized as follows: Roughly 80% of the $B\ ^3\Sigma_u^-$ state molecules are formed in $N'=4$ for each vibrational level, with the rest going into $N'=0$ [via $P_1(1)$] and $N'=2$ [via $^RQ_{32}(1)$]. Note that $N'\leqslant 4$ for all of these contributions. The $N'=4$ fine-structure populations are roughly proportional to the M' degeneracy of the original rotational quantum numbers J''. These degeneracies favor population of F_1, with the M'' degeneracies going as 9:7:5 for F_1, F_2, and F_3. For $v'=4$–11, the F_1 population was further enhanced because of the overlapped $P_1(1)$ transition, which accounted for 10%–15% of the total excitation. On the whole, though, the fine-structure populations of the excited rotational ensembles are largely statistical.

V. DISCUSSION

The correlated branching ratios $P_v(j_1,j_2)$ listed in Table I are the first observations of their kind for a light atom system. They contain information on both the detailed predissociation mechanism and the long-range dissociation dynamics. To model the branching ratios $P_v(j_1,j_2)$, we begin by breaking the problem down into two distinct regimes, short-range and long-range. In the short-range regime, the initial decay from the B state is controlled by the Franck–Condon overlap and spin–orbit coupling strength between the vibrational levels and the continuum scattering states of the four repulsive potentials shown in Fig. 1. This introduces a strong vibrational state dependence in the initial predissociation step. In Sec. V A, we review the quantitative description of the coupling of the prepared states with the repulsive states based on the findings of Chueng *et al.*[15,19] and of Lewis *et al.*[20] For our purposes, the primary result of Sec. V A will be the v-dependent branching ratios onto the four repulsive states.

The second half of the problem concerns how these repulsive states evolve in the long-range regime, ultimately projecting onto the asymptotic spin-orbit limits. The experimental results presented in this paper provide an interesting new perspective on this problem. In Sec. V B, we consider the interaction of these states as they evolve towards the atomic limit. Of primary importance is the role of nuclear kinetic energy in the evolution of the atoms along the disso-

ciative potentials. As a limiting case, we will first examine adiabatic behavior, i.e., what products may be expected for infinitely slow nuclear recoil. We will also examine the dissociation in the sudden approximation. Finally, we turn to a more phenomenological approach by finding the best fit for the projections of the repulsive states onto the asymptotic limits. We discuss what can be learned from the level of agreement between our simple predissociation models and the observed branching ratios $P_v(j_1,j_2)$.

A. Short-range dynamics

The basic nature of the predissociation mechanism was outlined in Sec. I. The high-resolution absorption data of Parkinson and co-workers[14,15,17] have provided our best window onto the nature of the short-range dissociation mechanism. These spectroscopic data hold a great deal of detailed information about the curve crossings, as reflected through the vibrational and rotational dependences of the linewidths and line shifts. These data have been collectively incorporated into semi-empirical models by Cheung *et al.*[15,19] and Lewis *et al.*[11,20] The semiempirical approach takes the best available *ab initio* calculations[28,35] of the curve crossing parameters R_x, M_x, and A_x and refines these values to improve agreement between modeled Franck–Condon predissociation widths and the experimental values. The perturbations to the term values of the observed vibrational progressions (induced by the spin–orbit couplings) are also taken into account. The most recent and most sophisticated effort to date is the recent work of Lewis *et al.*[20] They analyzed the detailed lineshapes by calculating the individual contributions of each of the (typically) unresolved spin–rotation components. By determining the fine-structure dependence of the natural linewidth one can learn more about which repulsive states dominate the predissociation.

In addition to an improved spectrum simulation and curve-crossing parameters, the results of the semiempirical fits provide a breakdown of each observed natural linewidth into a set of partial widths $\Gamma_k(v,N,F_i)$ that describe the decay rates into the available repulsive states.[54] Following Ref. 20, we will label the four repulsive states $2\ ^3\Sigma_u^+$, $^1\Pi_u$, $^3\Pi_u$, and $^5\Pi_u$ with $k=1-4$, respectively. Because the fitting procedure is not highly sensitive to some of the adjustable parameters, there may still be room for improvement in the model's results, particularly with respect to the $2\ ^3\Sigma_u^+$ and $^3\Pi_u$ widths. However, the overall level of agreement between the spectrum simulation of Lewis *et al.*[20] and the experimental data is of sufficiently high quality to ensure that the primary mechanism of the predissociation has been well described. If we neglect the N dependence of the partial widths $\Gamma_k(v,N,F_i)$ over the range from $0\leqslant N\leqslant 4$ (the range of N values contributing to each vibrational level v), the normalized predissociation rates along each repulsive curve k are given by

$$P_v(k)=\frac{\Sigma_{F_i} n_v(F_i)\Gamma_k(v,N=4,F_i)}{\Sigma_{k,F_i} n_v(F_i)\Gamma_k(v,N=4,F_i)}. \tag{9}$$

Here, $\Gamma_k(v,N=4,F_i)$ is obtained from Lewis *et al.*[20,54]

B. Long-range dynamics

Given that the predissociation mechanism has been fairly well elucidated from the absorption data, we now consider how the atoms, as they recoil along these four repulsive potentials, will project onto the six asymptotic fine-structure states. Two limiting descriptions of the evolution of the electronic state of the oxygen atoms, namely, the relativistic adiabatic and diabatic limits, will be discussed here. In the adiabatic limit it is assumed that after the initial curve crossing, the nuclei evolve on relativistic adiabatic potentials, defined below, all the way to the asymptotic limit.[33] This model of the dissociation is attractive because it is especially straightforward to predict product branching ratios. The relativistic adiabatic model was qualitatively successful in describing the $O(^3P_j)$ spin–orbit state distribution obtained by Huang and Gordon[36] following the $B\ ^3\Sigma_u^-$ continuum dissociation of O_2 at 157 nm. We present the predictions of this adiabatic model in Sec. V B *1*, and compare them to the observed spin–orbit distributions $P(j_1,j_2)$.

The diabatic (or ''sudden'') limit, on the other hand, is the projection of the repulsive states in the short-range, molecular regime onto the asymptotic, atomic limits without accounting for any electronic evolution during the course of the recoil. Thus, the initial Hund's case (a) basis functions $|S\Lambda\Omega\rangle$ for the four repulsive states are simply projected onto the atomic basis $|^3P_{j_1},^3P_{j_2}\rangle$ with care taken to conserve the g/u and $+/-$ symmetries as well as the total angular momentum J, its projection Ω, and the total electron spin S. In many cases, the coefficients of the transformation from the molecular Hund's case (a) basis to the atomic basis may be calculated without any detailed knowledge of the electronic structure; we will take advantage of this fact to make a qualitative analysis of product branching ratios in the diabatic limit in Sec. V B *2*.

1. Relativistic adiabatic limit

Following the outline given in Ref. 33, we consider the total Hamiltonian for a diatomic molecule

$$\mathbf{H}=\{\mathbf{H}^{\mathrm{el}}+\mathbf{H}^{\mathrm{so}}\}+\mathbf{T}^N. \tag{10}$$

Here, $\mathbf{H}^{\mathrm{el}}$ is the electronic part of Hamiltonian, consisting of the electrostatic potential (including $e-e$, $e-N$, and $N-N$) and electronic kinetic energy operators. $\mathbf{H}^{\mathrm{so}}$ represents the spin–orbit interaction (other relativistic terms are neglected), and $\mathbf{T}^N$ is the nuclear kinetic energy operator. The usual Born–Oppenheimer potentials $E_i^{\mathrm{BO}}(R)$ are derived from the solutions to the electronic Hamiltonian

$$\mathbf{H}^{\mathrm{el}}\Phi_i^{\mathrm{BO}}=E_i^{\mathrm{BO}}(R)\Phi_i^{\mathrm{BO}}, \tag{11}$$

where

$$\langle\Phi_i^{\mathrm{BO}}|\mathbf{H}^{\mathrm{el}}|\Phi_j^{\mathrm{BO}}\rangle=0 \quad \text{for all} \quad i\neq j. \tag{12}$$

The functions $E_i^{\mathrm{BO}}(R)$ will cross freely unless all of the quantum numbers Λ, S, and Ω are shared between two states. In this basis, at short R, the diagonal spin–orbit interaction is treated in a phenomenological fashion by approximating it to

TABLE II. Adiabatic correlations between the ground state atomic limit $O(^3P_{j_1})$, $O(^3P_{j_2})$ and O_2 molecular states. The states are energy ordered, with the bottom of the table corresponding to the most stable states.

Atomic limit (j_1,j_2)	Ω	$n(\Omega)$[a]	*Ungerade* states		*Gerade* states	
			Ω	Molecular correlations	Ω	Molecular correlations
(0,0)	0^-	}1				
	0^+				0_g^+	$2\ ^5\Sigma_g^+$
(1,0)+	1	4	1_u	$2\ ^3\Sigma_u^+$	1_g	$2\ ^5\Sigma_g^+$
(0,1)	0^-	}2	0_u^-	$2\ ^3\Sigma_u^+$	0_g^-	$^5\Delta_g$
	0^+					
	2	2			2_g	$2\ ^5\Sigma_g^+$
(1,1)	1	4	1_u	$^5\Pi_u$	1_g	$^5\Delta_g$
	0^-	}3	0_u^-	$^5\Pi_u$		
	0^+				$0_g^+,0_g^+$	$^5\Delta_g,2\ ^1\Sigma_g^+$
	2	4	2_u	$^5\Pi_u$	2_g	$^5\Delta_g$
(2,0)+	1	4	1_u	$^5\Pi_u$	1_g	$^5\Sigma_g^+$
(0,2)	0^-	}2				
	0^+		0_u^+	$^5\Pi_u$	0_g^+	$^5\Sigma_g^+$
	3	4	3_u	$^5\Pi_u$	3_g	$^5\Delta_g$
(2,1)+	2	8	$2_u,2_u$	$^3\Pi_u,^5\Sigma_u^-$	$2_g,2_g$	$^5\Pi_g,^5\Sigma_g^+$
(1,2)	1	12	$1_u,1_u,1_u$	$^3\Pi_u,^1\Pi_u,^5\Sigma_u^-$	$1_g,1_g,1_g$	$^1\Pi_g,^5\Pi_g,^5\Pi_g$
	0^-	}6	$0_u^-,0_u^-$	$^3\Pi_u,^5\Sigma_u^-$	$0_g^-,0_g^-$	$^3\Pi_g,^5\Pi_g$
	0^+		0_u^+	$^3\Pi_u$	0_g^+	$^5\Pi_g$
	4	2			4_g	$^5\Delta_g$
	3	4	3_u	$A'\ ^3\Delta_u$	3_g	$^5\Pi_g$
(2,2)	2	6	2_u	$A'\ ^3\Delta_u$	$2_g,2_g$	$a\ ^5\Delta_g,^3\Pi_g$
	1	8	$1_u,1_u$	$A'\ ^3\Delta_u,A\ ^3\Sigma_u^+$	$1_g,1_g$	$X\ ^3\Sigma_g^-,^3\Pi_g$
	0^-	}5	$0_u^-,0_u^-$	$c\ ^1\Sigma_u^-,A\ ^3\Sigma_u^+$		
	0^+				$0_g^+,0_g^+,0_g^+$	$X\ ^3\Sigma_g^-,b\ ^1\Sigma_g^+,^3\Pi_g$

[a]$n(\Omega)$ is the total number of molecular states with $J_z=\Omega$ that correlate to the indicated asymptotic limit. Note that states with $\Omega\neq 0$ are doubly degenerate.

be R independent. Thus curves $E_i^{\mathrm{BO}}(R)$ differing only in Ω are shifted relative to one another by an R-averaged, Ω-specific spin–orbit energy.

An alternative ''relativistic'' basis is produced when we include the relativistic part of the Hamiltonian, with a new set of curves $E_i^{\mathrm{rel}}(R)$

$$\{\mathbf{H}^{\mathrm{el}}+\mathbf{H}^{\mathrm{so}}\}\Phi_i^{\mathrm{rel}}=E_i^{\mathrm{rel}}(R)\Phi_i^{\mathrm{rel}}. \tag{13}$$

For these states, only Ω is a good quantum number, and the curves $E_i^{\mathrm{rel}}(R)$ will always avoid crossing at intersections of common Ω. While avoided crossings between the Born–Oppenheimer potentials $E_i^{\mathrm{BO}}(R)$ arise infrequently, the same cannot be said for the relativistic potentials $E_i^{\mathrm{rel}}(R)$.

In light-atom molecules, the spin–orbit coupling is weak, and typical short-range curve crossings carry only a small probability for relativistic adiabatic behavior. Such is the case for the intersection between the B state and the four repulsive curves. At longer range, on the other hand, the Born–Oppenheimer potentials may be nearly parallel at their intersection, and the probability for adiabatic following at an avoided crossing is higher. In the limit of the recoiling atoms moving infinitely slowly through an intersection (adiabatic limit), the weakest of spin–orbit interactions between the crossing Born–Oppenheimer curves with common Ω will give rise to a perfectly avoided crossing. In the framework of the adiabatic basis, the central question is how the nuclear kinetic energy operator $\mathbf{T}^N$ will couple the adiabatic potentials. While the extent of this coupling at long range is unknown, it is quite useful to examine the fully relativistic adiabatic limit, and find what predictions can be made about the dissociation products.

The most attractive feature of the relativistic adiabatic model is that a one-to-one mapping of the molecular electronic states to asymptotic (j_1,j_2) states can easily be constructed.[36] Because adiabatic curves with the same Ω never cross, the energy ordering of these states is preserved from short range to the atomic limit. In Table II we display (with the aid of *ab initio* electronic structure calculations[28]) the short-range energy ordering for the *ungerade* states of O_2 that correlate to the ground state $O(^3P_j)+O(^3P_j)$ limit. The contents of Table II are essentially identical to those of Fig. 8 in the paper of Huang and Gordon.[36] Establishing the same sort of ordering for the atomic limits is also a straightforward task with a few minor complications. The 81 states in the ground state limit can each be classified as *gerade* or *ungerade*; furthermore, the $\Omega=0$ states have $+/-$ parity. These classifications are carried out using the Wigner–Witmer rules, which are summarized by Herzberg.[55] Since g/u symmetry should be conserved throughout the dissociation process, regardless of whether dissociation is adiabatic or not, no $(j_1=0,\ j_2=0)$ products should be formed from predissociation of the $B\ ^3\Sigma_u^-$ state because this final state has g symmetry; this is borne out by our experimental results.

The adiabatic treatment of the $B\ ^3\Sigma_u^-$ state predissociation is further simplified because we assume Ω conservation to hold at all internuclear distances R. The only mechanisms

TABLE III. Adiabatic correlation coefficients $C^{ad}(j_1,j_2;k)$ based on the correlations of Table II.

k	(2,2)	(2,1)	(2,0)	(1,1)	(1,0)
1 ($2\ ^3\Sigma_u^+$)	0	0	0	0	1
2 ($^1\Pi_u$)	0	1	0	0	0
3 ($^3\Pi_u$)	0	1	0	0	0
4 ($^5\Pi_u$)	0	0	2/3	1/3	0

that mix Ω (beyond S uncoupling) are weak for low J, and become rapidly weaker as the molecule dissociates.[20] The $B\ ^3\Sigma_u^-$ state has only $\Omega=0^+$ and 1 components, so only those states in Table II with $\Omega=0^+$ and 1 (and with u symmetry) will participate. In this way, of the original 81 atomic states, symmetry constraints dictate that only 18 need be considered here. Thus for example, the accessible Ω components of the $^3\Pi_u$ state all correlate adiabatically to the ($j_1=2$, $j_2=1$) limit.

With the aid of the semiempirical partial predissociation widths $P_v(k)$ [Eq. (9)] and the correlation diagram of Table II, we can predict the correlated spin–orbit distributions $P_v^{ad}(j_1,j_2)$ *in the adiabatic limit*

$$P_v^{ad}(j_1,j_2)=\sum_k P_v(k)C^{ad}(j_1,j_2;k). \tag{14}$$

As mentioned earlier, k labels the four repulsive states $2\ ^3\Sigma_u^+$, $^1\Pi_u$, $^3\Pi_u$, and $^5\Pi_u$. With the exception of the $^5\Pi_u$ state ($k=4$), the correlation coefficients $C^{ad}(j_1,j_2;k)$ are either one or zero depending on whether or not the repulsive curve k correlates adiabatically to the limit (j_1,j_2) (Table II). The $\Omega=1$ component of the $^5\Pi_u$ state (with $\Sigma=0$) correlates adiabatically to both the (2,0) limit and the (1,1) limit, while its $\Omega=0^+$ component correlates to the (2,0) limit. To account for this, we assume the doubly degenerate $\Omega=1$ component to be divided evenly between the two limits, and that the $\Omega=1$ and $\Omega=0^+$ components of each vibrational level are present in a 2:1 ratio. This yields $C^{ad}(1,1;4)=1/3$ and $C^{ad}(2,0;4)=2/3$. The $C^{ad}(j_1,j_2;k)$ coefficients are listed in Table III.

The results given by Eq. (14) are shown along with the experimental data in Fig. 7. Agreement between $P_v^{ad}(j_1,j_2)$ and experiment is poor. The most spectacular failure of the adiabatic model concerns the ground state (2,2) limit. All of the (2,2) *ungerade* atomic limits correlate exclusively to the three strongly bound O_2 *ungerade* states. As such, the (2,2) limit is not adiabatically correlated to *any* of the repulsive states involved in the predissociation of the $B\ ^3\Sigma_u^-$ state. However, despite being forbidden in the adiabatic limit, ground state products are formed in abundance following the predissociation of the lowest vibrational levels of the $B\ ^3\Sigma_u^-$ state, peaking at 33% for $v'=1$. At this recoil energy ($\sim$1 eV), the motion of the atoms is apparently fast enough for transitions to occur at avoided crossings between relativistic adiabatic curves. Because the adiabatic model represents the slow recoil limit, the applicability of the model can only degrade for $v'>1$. The conclusion to be drawn from Fig. 7 is that the nuclear kinetic energy is in general too high for dissociation to proceed adiabatically.

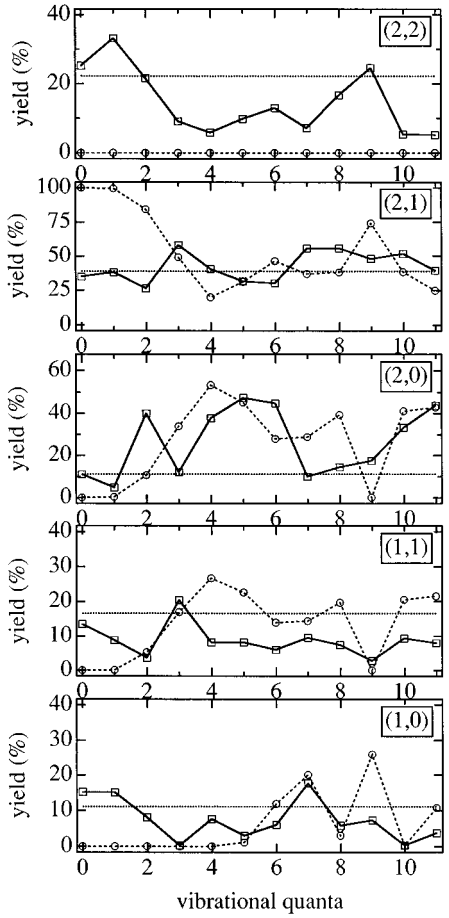

FIG. 7. Predicted correlated fine structure distributions as function of $B\ ^3\Sigma_u^-$ vibrational quantum number using adiabatic model [Eq. (14)] compared to experimental results. The model is represented as circles, and the experimental data points are squares.

2. Diabatic limit

Diametrically opposed to the relativistic adiabatic approximation is the sudden or diabatic limit. In this approximation, it is assumed that the nuclei progress through curve crossings so quickly that the electronic wavefunction has no opportunity to change its configuration and avoid the crossing. Rather than consider what happens at each avoided crossing, we consider the limit where the Born–Oppenheimer states $|\Lambda S\Omega\rangle$ [i.e., the solutions to Eq. (11)] on which predissociation occurs at short range are projected suddenly onto the atomic limit, conserving Λ and S in addition to Ω.

While the sudden limit sounds straightforward, it is somewhat awkward to apply, because the Born–Oppenheimer potentials do not correlate in a simple way to the atomic limits (j_1,j_2). Instead, a given Born–Oppenheimer state $|\Lambda S\Omega\rangle$ will form a superposition of atomic states as dictated by angular momentum coupling and in many cases by the electronic structure. This problem has been addressed in considerable detail by Singer *et al.*[56] The matrix elements for the transformation from the molecular basis to the atomic limit presented in Ref. 56 are reproduced here. We then derive the correlated spin–orbit cross sections expected in this limit.

We wish to find the projection of the molecular basis $|\Lambda S\Omega\rangle$ into the atomic basis $|j_1,j_2\rangle$. The matrix element given in Eq. (II.13a) of Ref. 56 as it appears for our application (^3P_j atoms: $l_1=l_2=s_1=s_2=1$) is

$$\begin{aligned}\langle jlj_1j_2|\Lambda S\Omega\rangle_J=&(-1)^{l-\Omega-J}[(2S+1)(2j_1+1)\\&\times(2j_2+1)]^{1/2}\langle l0|j-\Omega,J\Omega\rangle\\&\times\sum_{L\lambda_1\lambda_2}\frac{[1-\delta_{j_1j_2}(-1)^L]^{1/2}}{2^{1/2}}(2L+1)^{1/2}\\&\times\langle L\Lambda|1\lambda_1,1\lambda_2\rangle\langle j\Omega|L\Lambda,S\Sigma\rangle\\&\times\begin{Bmatrix}1&1&j_1\\1&1&j_2\\L&S&j\end{Bmatrix}\langle\lambda_1,\lambda_2|\Lambda\rangle.\end{aligned}\tag{15}$$

In this equation, j represents the vector sum of the atomic total angular momenta j_1 and j_2, l is the orbital angular momentum of the recoiling oxygen atoms, λ_1 and λ_2 are the projections of the electronic orbital angular momentum of the atoms, l_1 and l_2, and L is the total electronic orbital angular momentum. The *ungerade* symmetry of the molecular state manifests itself in two different ways in the atomic limit. When $j_1\neq j_2$, exactly half of the asymptotic states are *ungerade*, and the $2^{1/2}$ divisor in the sum accounts for this. When $j_1=j_2$, the nuclear permutation eigenvalue is given by $(-1)^L$; the factor of $[1-\delta_{j_1j_2}(-1)^L]^{1/2}$ limits the summand to *ungerade* states ($L=$odd) and cancels the aforementioned $2^{1/2}$ divisor. The electronic overlap terms $\langle\lambda_1,\lambda_2|\Lambda\rangle$ hold the R dependence of the transformation, converging to some limiting value as $R\to\infty$. For the three $^{2S+1}\Pi_u$ states under consideration ($S=0$, 1, and 2), the only such terms are the symmetric $\langle 0,1|1\rangle$ and $\langle 1,0|1\rangle$ terms, and the diabatic coupling to the atomic limits can be calculated directly. On the other hand, electronic structure calculations are required to determine the $\langle 0,0|0\rangle$ and $\langle 1,-1|0\rangle$ terms for the diabatic coupling of the $2\ ^3\Sigma_u^+$ state to the atomic limit. However, we will take $\langle 0,0|0\rangle=\langle 1,-1|0\rangle$ to calculate approximate couplings for the $2\ ^3\Sigma_u^+$ state.

The diabatic transformation cross sections to the asymptotic limit $|j_1,j_2\rangle$ are found by summing coherently over the unobserved momenta j and l

$$C^d(j_1,j_2;k\Omega)=\left|\sum_{j,l}\langle jlj_1j_2|\Lambda S\Omega\rangle_{J=4}\right|^2.\tag{16}$$

This gives the expected diabatic branching ratio for a single dissociation pathway. However, the predissociation of O_2 can be thought of as a four-slit experiment, where a given Ω component of a B state rotational level will connect to each (j_1,j_2) product state via up to four available pathways, namely, the $^5\Pi_u$, $^3\Pi_u$, $^1\Pi_u$, and $2\ ^3\Sigma_u^+$ repulsive states. The relative phases of these pathways must be taken into account to calculate the total amplitudes of the product scattering states. These phases, which depend on the initial vibrational level v, are unknown, precluding a completely quantitative analysis of the diabatic limit. As a crude approximation, we will sum the diabatic contributions as they appear in Eq. (16) incoherently

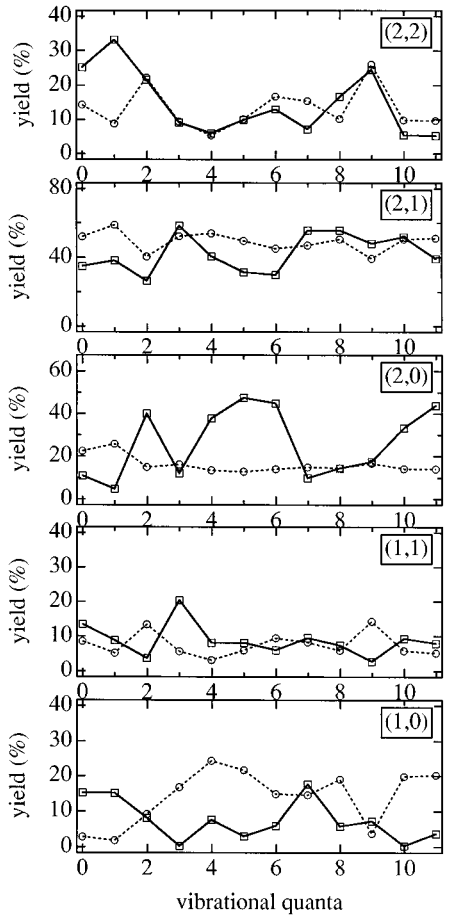

FIG. 8. Predicted correlated fine structure distributions as function of $B\ ^3\Sigma_u^-$ vibrational quantum number using adiabatic model [Eq. (17)] compared to experimental results. The model is represented as circles, and the experimental data points are squares.

$$P_v^d(j_1,j_2)\approx\sum_{k,\Omega=0,\pm1}P_v(k)C^d(j_1,j_2;k\Omega).\tag{17}$$

In the case of rovibrational levels that decay primarily via one surface (e.g., $v=1$ and 4), Eq. (17) will be correspondingly less approximate (within the overall sudden approximation). The resulting diabatic branching ratios $P_v^d(j_1,j_2)$ are shown along with the experimental data in Fig. 8. Unlike the adiabatic limit, the diabatic model predicts a significant yield in the ground state (2,2) channel. In fact, the diabatic model does a good job of reproducing the v' dependence observed experimentally for this channel, particularly at high v', where the the photofragment kinetic energy should yield more diabatic behavior. On the whole, though, the agreement between model and experiment is once again less than satisfactory. Even for $v'=1$ and $v'=4$, which dissociate with over 75% efficiency into the $^1\Pi_u$ and $^5\Pi_u$ continua, respectively, the diabatic model appears to have little predictive power, with significant discrepancies in the (2,0) and (1,0) channels.

The conclusions to be drawn from Fig. 8 are not so clear as those from Fig. 7. It may well be that the dissociation is largely diabatic, and that the discrepancies between model and experiment in Fig. 8 arise from our neglect of interfer-

TABLE IV. Best linear fit coefficients $a(j_1,j_2;k)$ of the partial predissociation widths of Lewis *et al.* to the observed product state distributions $P_v(j_1,j_2)$.

k	(2,2)	(2,1)	(2,0)	(1,1)	(1,0)
1 ($2\ ^3\Sigma_u^+$)	0	0.78	0	0	0.22
2 ($^1\Pi_u$)	0.27	0.47	0	0.15	0.11
3 ($^3\Pi_u$)	0.26	0.22	0.42	0.01	0.09
4 ($^5\Pi_u$)	0	0.54	0.31	0.15	0

ence effects. On the other hand, the dissociation may lie between the adiabatic and diabatic limits. It is possible that one can understand the dissociation dynamics of O_2 within the confines of a reasonably simple combination of adiabatic and diabatic processes. Durup[57] has analyzed the predissociation of O_2^+ to form $O^+(^4S)+O(^3P_j)$, and constructed a ''mixed diabatic basis'' which was quite useful in modeling the observed j distribution of the $O(^3P)$ atom. In this basis, some of the dissociative states are found to be largely adiabatic, while others are predominantly diabatic. The assumption of pure adiabatic behavior for the former and pure diabatic behavior for the latter yields reasonable, although not perfect, agreement with the experimental fine-structure distributions. Whether such a basis can be constructed for predissociation of the $O_2B\ ^3\Sigma_u^-$ state remains to be seen.

3. Least-squares fit branching ratios

The results in the previous section show that neither the adiabatic nor diabatic limits describe our data very well. In this section, we apply a more phenomenological approach to our data in which we find the set of coefficients analogous to those in Table III that provide the best fit to the data. We assume that each of the four repulsive states maps onto the product states (j_1,j_2) independently of v or Ω for the predissociating state. We then require 20 coefficients describing the branching of each repulsive state k into the five product states (j_1,j_2). These branching ratios are expressed as the elements of the array $a(j_1,j_2;k)$, subject to the normalization conditions

$$\sum_k a(j_1,j_2;k)=1. \tag{18}$$

The linear coefficients $a(j_1,j_2;k)$ are fit to the observed $P_v(j_1,j_2)$ for all 12 vibrational levels simultaneously, comprising a system of 60 equations of the form

$$P_v(j_1,j_2)=\sum_k P_v(k)a(j_1,j_2;k). \tag{19}$$

The form of Eq. (19) is identical to Eq. (14) with the exception that the correlation coefficients are now treated as adjustable parameters.

The results of the least-squares fit are given in Table IV and shown in Fig. 9. In the fit, it was necessary to impose a non-negativity constraint for many of the coefficients $a(j_1,j_2;k)$; these coefficients appear as zeroes in the table. The level of agreement of this phenomenological treatment with the experimental data represents a significant improvement over both the adiabatic and diabatic limits. This is not too surprising, given the large number of parameters used in the fit. However, the reduced χ^2 of the fit was 37, indicating that this model of v-independent branching ratios is not consistent with the data given the precision of the measurements. Figure 8 shows that the fit does quite well for the (2,2) channel, somewhat less well for the (1,1) and (1,0) channels, and gives the poorest results for the (2,1) and (2,0) channels where it fails to reproduce the oscillatory structure with v seen in the experiment. Such structure may reflect quantum interference between competing decay paths, leading to a vibrational dependence in the branching coefficients $a(j_1,j_2;k)$. Alternatively, the v dependence of the dissociation mechanism may occur simply because the kinetic energy is increasing with increasing v, thereby affecting the coupling at long-range between the molecular and atomic states.

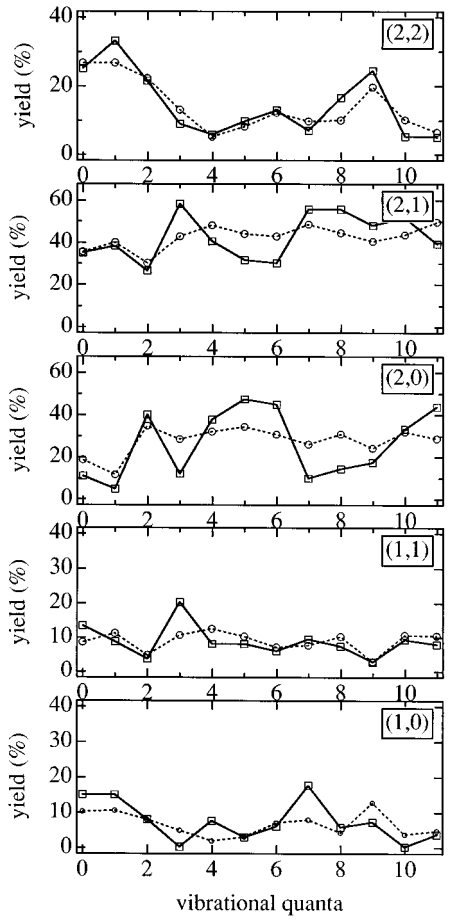

FIG. 9. Predicted correlated fine structure distributions as function of $B\ ^3\Sigma_u^-$ vibrational quantum number using adiabatic model [Eq. (19)] compared to experimental results. The model is represented as circles, and the experimental data points are squares.

Nonetheless, the coefficients in Table IV reflect the pathway specific branching ratios in, at the very least, a v-averaged sense. It is instructive to compare these coefficients with those in Table III, because there are some patterns shared between the adiabatic correlation coefficients $C^{\mathrm{ad}}(j_1,j_2;k)$ of Table III and the $a(j_1,j_2;k)$ of Table IV. In Table III, no states correlate with the (2,2) products, while the $^3\Pi_u$ and $^1\Pi_u$ states correlate with the (2,1) channel. In Table IV, only the $^3\Pi_u$ and $^1\Pi_u$ states lead to (2,2) products.

This is the result that would be expected in the case where adiabatic limit is relaxed slightly, in which case molecules would begin to transfer into neighboring limits by making single curve hops. Such a result is consistent with the experiment. Figure 7 shows that the observed (2,2) branching ratio is about 0.3 times the adiabatic prediction for the (2,1) channel for all v; this scaling suggests that the (2,2) channel is due to nonadiabatic transitions from states that adiabatically correlate to the neighboring (2,1) channel. Also, in the adiabatic model, the $2\ ^3\Sigma_u^+$ state is the only one that correlates to the (1,0) product, while in the linear fit, the largest contribution to the (1,0) product also comes from this state. Thus the degree of nonadiabaticity may not sufficient to completely scramble the adiabatic correlations, so that the impression of the adiabatic correlation may still be found in the data. On the other hand, a comparison of Tables III and IV implies that multiple hopping between adiabatic curves is required to explain the observed branching ratios for the other three channels.

Overall, it appears that an exact dynamical calculation, probably including quantum interference effects, on high quality potential energy curves is required to match the experimental results. Given that single transitions between relativistic adiabatic potentials can partly explain the dissociation dynamics, it may be preferable to use the relativistic adiabatic states as a basis for this calculation. To our knowledge, a multichannel calculation of this type has not been performed yet, and we hope that our results stimulate theoretical activity in this area.

4. Comparison to earlier results

The correlated fine-structure distributions in Table I have not been measured previously. However, Matsumi and Kawasaki (hereafter referred to as MK) have used multiphoton ionization to measure the *un*correlated spin–orbit distribution $P(j)$ following the predissociation of the $B\ ^3\Sigma_u^-$ state $v'=4$ level with 193 nm light.[37] They observed atoms in $j=2$, 1, and 0 in the ratio of 0.47(5):0.31(4):0.22(4), respectively. Casting our results for $v'=4$ into uncorrelated ratios, we obtain the ratio 0.451(15):0.323(14):0.227(11), in excellent agreement with MK.

In the same paper, MK presented results for the 157 nm photodissociation of the $B\ ^3\Sigma_u^-$ state to the excited $O(^1D)$, $O(^3P_j)$ limit. At this wavelength, one is accessing the repulsive wall of the $B\ ^3\Sigma_u^-$ state (see Fig. 1), so direct dissociation rather than predissociation is occurring. MK report the $P(j)$ distribution at 157 nm to be 0.74:0.21:0.04. In another experiment at 157 nm, Huang and Gordon (HG) reported a substantially different $P(j)$ distribution, 0.93:0.06:0.01,[36] using laser-induced fluorescence to measure O atom populations. HG suggested that the MK result was in error because of amplified spontaneous emission affecting Kawasaki's detection scheme.[36,58] However, the close agreement between our results and those of MK for the $v'=4$ level shows that their detection scheme at 193 nm is reliable. This suggests, albeit indirectly, that MK's results at 157 nm are also correct. This conclusion is significant because the nascent $O(^3P_j)$ atom spin–orbit distribution from the atmospheric dissociation of O_2 depends strongly on photodissociation dynamics in the 157 nm range.

The discrepancy between the two sets of data at 157 nm is also important from the perspective of adiabaticity in the dissociation process. Adiabatically, the $B\ ^3\Sigma_u^-$ state correlates to the $O(^3P_2)+O(^1D)$ limit. Thus HG concluded that the dissociation is largely adiabatic, whereas MK's results indicate considerably larger nonadiabatic effects. Our results have clearly demonstrated the importance of nonadiabatic effects in predissociation of the $B\ ^3\Sigma_u^-$ state to form $O(^3P_j)+O(^3P_j)$. Given that the densities of states at long range for the two atomic limits are similar, and that the translational energy of the O atoms is $\sim$1 eV in both our experiment and those at 157 nm, one might certainly expect nonadiabatic effects to be important at 157 nm as well, in contrast to the results of HG. It is certainly true that we are observing the products from predissociation on multiple repulsive potentials at short range, whereas dissociation is direct at 157 nm. Nonetheless, the agreement of our results with those of MK at lower energy suggests that the notion of adiabatic dissociation at 157 nm should be re-examined.

VI. CONCLUSIONS

High resolution translational energy release spectra of the $O(^3P_j)$ atoms resulting from O_2 $B\ ^3\Sigma_u^-$ predissociation have been recorded for $0\leqslant v\leqslant 11$. The spectra yield a relatively unexplored (both experimentally and theoretically) observable, namely, the correlated fine structure state distributions $P_v(j_1,j_2)$. These show a strong dependence on the vibrational quantum number v of the predissociating level. The details of the predissociation mechanism are presented to provide a basis for the analysis of spin–orbit distributions. Two limiting descriptions of the evolution of the nuclei from molecule to atoms are discussed. The predictions of the relativistic adiabatic limit and the sudden limit both fail to reproduce the v dependence of the observed spin–orbit distributions. We have also performed a phenomenological least-squares fit in which the branching ratios of each repulsive states to the various product states are determined. This yields more insight into the long-range ($R\approx 5$–7 Å) dynamics of the dissociation and suggests that while the dissociation lies in a complex intermediate regime, a residual impression of adiabatic behavior persists in the data. It appears that a full quantum dynamical calculation on accurate potential energy curves will be necessary to reproduce our experimental results.

ACKNOWLEDGMENTS

The authors acknowledge the contributions of David H. Mordaunt to the data collection effort. This research is supported by the Director, Office of Energy Research, Office of Basic Energy Sciences, Chemical Sciences Division, of the U.S. Department of Energy under Contract No. DE-AC03-76SF00098.

[1] V. Schumann, Smithson. Contrib. Knowl. **29**, 1413 (1903).
[2] C. Runge, Physica **1**, 254 (1921).
[3] J. Curry and G. Herzberg, Ann. Phys. **19**, 800 (1934).
[4] P. Brix and G. Herzberg, Can. J. Phys. **32**, 110 (1954).

[5] P. G. Wilkinson and R. S. Mulliken, Astrophys. J. **125**, 594 (1957).
[6] P. K. Carroll, Astrophys. J. **129**, 794 (1959).
[7] M. Ackerman and F. Biaumé, J. Mol. Spectrosc. **35**, 73 (1970).
[8] P. H. Krupenie, J. Phys. Chem. Ref. Data **1**, 423 (1972).
[9] R. D. Hudson and S. H. Mahle, J. Geophys. Res. **77**, 2902 (1972). P.
[10] D. M. Creek and R. W. Nicholls, Proc. R. Soc. London, Ser. A **341**, 517 (1975).
[11] B. R. Lewis, L. Berzins, J. H. Carver, and S. T. Gibson, J. Quant. Spectrosc. Radiat. Transfer **36**, 187 (1986).
[12] B. R. Lewis, J. H. Carver, T. I. Hobbs, D. G. McCoy, and H. P. F. Gies, J. Quant. Spectrosc. Radiat. Transfer **20**, 191 (1978); **22**, 213 (1979); H. P. F. Gies, S. T. Gibson, D. G. McCoy, A. J. Blake, and B. R. Lewis, *ibid*. **26**, 469 (1981).
[13] A. M. Wodtke, L. Huwel, H. Schluter, H. Voges, G. Meijer, and P. Andresen, J. Chem. Phys. **89**, 1929 (1988).
[14] A. S.-C. Cheung, K. Yoshino, D. E. Freeman, and W. H. Parkinson, J. Mol. Spectrosc. **131**, 96 (1988); A. S-C. Cheung, K. Yoshino, D. E. Freeman, R. S. Friedman, A. Dalgarno, and W. H. Parkinson, *ibid*. **134**, 362 (1989); S. S-L. Chiu, A. S-C. Cheung, K. Yoshino, J. R. Esmond, D. E. Freeman, and W. H. Parkinson, J. Chem. Phys. **93**, 5539 (1990).
[15] A. S-C. Cheung, K. Yoshino, J. R. Esmond, S. S.-L. Chiu, D. E. Freeman, and W. H. Parkinson, J. Chem. Phys. **92**, 842 (1990).
[16] X. Yang, A. M. Wodtke, and L. Hüwel, J. Chem. Phys. **94**, 2469 (1991).
[17] K. Yoshino, J. R. Esmond, A. S.-C. Cheung, D. E. Freeman, and W. H. Parkinson, Planet. Space Sci. **40**, 185 (1992).
[18] P. C. Cosby, H. Park, R. A. Copeland, and T. G. Slanger, J. Chem. Phys. **98**, 5117 (1993).
[19] A. S.-C. Cheung, D. K-W. Mok, M. J. Jamieson, M. Finch, K. Yoshino, A. Dalgarno, and W. H. Parkinson, J. Chem. Phys. **99**, 1086 (1993).
[20] B. R. Lewis, S. T. Gibson, and P. M. Dooley, J. Chem. Phys. **100**, 7012 (1994).
[21] P. J. Flory, J. Chem. Phys. **4**, 23 (1936).
[22] I. M. Campbell and C. N. Gray, Chem. Phys. Lett. **18**, 607 (1973).
[23] P. C. Wraight, Planet. Space Sci. **30**, 251 (1982).
[24] I. W. M. Smith, Int. J. Chem. Kinet. **16**, 423 (1984).
[25] D. R. Bates, Planet. Space Sci. **37**, 881 (1989), and references therein.
[26] D. R. Bates, Chem. Phys. Lett. **162**, 313 (1989).
[27] R. L. Miller, A. G. Suits, P. L. Houston, R. Toumi, J. A. Mack, and A. M. Wodtke, Science **265**, 1831 (1994).
[28] H. Partridge, C. W. Bauschlicher, Jr., S. R. Langhoff, and P. R. Taylor, J. Chem. Phys. **95**, 8292 (1991).
[29] W. J. van der Zande, W. Koot, J. Los, and J. R. Peterson, J. Chem. Phys. **89**, 6758 (1988).
[30] P. C. Cosby and H. Helm, J. Chem. Phys. **90**, 1434 (1989).
[31] J. N. Murrell and J. M. Taylor, Mol. Phys. **16**, 609 (1969).
[32] H. F. Schaefer and W. H. Miller, J. Chem. Phys. **55**, 4107 (1971).
[33] H. Lefebvre-Brion and R. W. Field, *Perturbations in the Spectra of Diatomic Molecules* (Academic, Orlando, 1986), pp. 29–51.
[34] P. S. Julienne and M. Krauss, J. Mol. Spectrosc. **56**, 270 (1975).
[35] P. S. Julienne, J. Mol. Spectrosc. **63**, 60 (1976).
[36] Y. L. Huang and R. J. Gordon, J. Chem. Phys. **94**, 2640 (1990).
[37] Y. Matsumi and M. Kawasaki, J. Chem. Phys. **93**, 2481 (1990).
[38] K. Tonokura, N. Shafer, Y. Matsumi, and M. Kawasaki, J. Chem. Phys. **95**, 3394 (1991).
[39] D. J. Leahy, D. R. Cyr, D. L. Osborn, and D. M. Neumark, Chem. Phys. Lett. **216**, 503 (1993).
[40] R. E. Continetti, D. R. Cyr, D. L. Osborn, D. J. Leahy, and D. M. Neumark, J. Chem. Phys. **99**, 2616 (1993).
[41] L. A. Posey, M. J. Deluca, and M. A. Johnson, Chem. Phys. Lett. **131**, 170 (1986).
[42] R. E. Continetti, D. R. Cyr, and D. M. Neumark, Rev. Sci. Instrum. **63**, 1840 (1992).
[43] J. M. B. Bakker, J. Phys. E **6**, 785 (1973); **7**, 364 (1974).
[44] R. J. Celotta, R. A. Bennett, J. L. Hall, M. W. Siegel, and J. Levine, Phys. Rev. A **6**, 631 (1972).
[45] M. J. Travers, D. C. Cowles, and G. B. Ellison, Chem. Phys. Lett. **164**, 449 (1989).
[46] D. P. de Bruijn and J. Los, Rev. Sci. Instrum. **53**, 1020 (1982).
[47] O. H. W. Siegmund, M. Lampton, J. Bixler, S. Bowyer, and R. F. Malina, IEEE Trans. Nucl. Sci. **NS-33**, 724 (1986); J. V. Vallerga, G. C. Kaplan, O. H. W. Siegmund, M. Lampton, and R. F. Malina, *ibid*. **NS-36**, 881 (1989).
[48] P. C. Cosby and D. L. Huestis, J. Chem. Phys. **97**, 6109 (1992).
[49] W. H. Press, B. P. Flannery, S. A. Teukolsky, and W. T. Vettering, *Numerical Recipes* (Cambridge University, Cambridge, 1986), pp. 523–528.
[50] D. R. Cyr, D. J. Leahy, D. L. Osborn, R. E. Continetti, and D. M. Neumark, J. Chem. Phys. **99**, 8751 (1993).
[51] D. L. Osborn, D. J. Leahy, E. M. Ross, and D. M. Neumark, Chem. Phys. Lett. **235**, 484 (1995).
[52] C. E. Moore, *Atomic Energy Levels*, Vol. 1, NSRDS-NBS Circ. No. 467 (U.S. GPO, Washington, 1949), p. 15.
[53] J. B. Tatum and J. K. G. Watson, Can. J. Phys. **49**, 2693 (1971).
[54] B. R. Lewis, private communication. Only a small subset of these partial linewidths are given in Ref. 20.
[55] G. Herzberg, *Molecular Spectra and Molecular Structure* (Van Nostrand, New York, 1950), pp. 315–322.
[56] S. J. Singer, K. F. Freed, and Y. B. Band, J. Chem. Phys. **79**, 6060 (1983).
[57] J. Durup, Chem. Phys. **59**, 351 (1981).
[58] Y.-L. Huang and R. J. Gordon, J. Chem. Phys. **97**, 6363 (1992).